



Trans. Nonferrous Met. Soc. China 34(2024) 2074-2094

Transactions of Nonferrous Metals Society of China

www.tnmsc.cn



Numerical simulation on metallic droplet deformation and breakup concerning particle morphology and hollow particle formation during gas atomization

Peng WANG^{1,2}, Xing-gang LI³, Xiang-lin ZHOU¹, Zhi-pei CHEN⁴, Miao-hui WANG², Ping GAN², Xiao-na REN⁴, Zhi-yong YU⁵

1. State Key Laboratory for Advanced Metals and Materials, University of Science and Technology Beijing, Beijing 100083, China;

2. China Machinery Institute of Advanced Materials (Zhengzhou) Co., Ltd., Zhengzhou 450001, China;

3. Department of Materials Science and Engineering,

Southern University of Science and Technology, Shenzhen 518055, China;

4. School of Materials Science and Engineering,

University of Science and Technology Beijing, Beijing 100083, China;

5. China United Gas Turbine Technology Co., Ltd., Beijing 100016, China

Received 19 April 2023; accepted 14 November 2023

Abstract: The deformation and breakup of metallic droplets during gas atomization were simulated using a volume of fluid (VOF) approach that considered droplet cooling and solidification. The correlation between the typical powder morphology and droplet breakup behavior was established to guide the preparation of spherical powder particles. The results showed that upon increasing the ratio of aerodynamic to viscous force of the droplet, the formation of spherical particles was enhanced, while upon decreasing this ratio, the expected droplet breakup mode changed or only droplet deformation occurred. Several typical scenarios were observed from the numerical simulations of the hollow particle formation and evolution process, e.g., open hollow film formation, film closure, bubble centrifugation, and bubble detachment. By increasing the gas velocity or droplet temperature, a higher non-equilibrium Laplace pressure or lower viscous forces was achieved, which separated the bubbles from the interior of the droplet.

Key words: droplet breakup; hollow particle; particle morphology; viscous force; metal powder; gas atomization

1 Introduction

Metal additive manufacturing (MAM) has been rapidly developed in recent years and prevails over conventional subtractive approaches because it allows for the rapid on-demand production of more complex parts with lower energy consumption and costs [1–3]. Nevertheless, MAM uses specially-tailored metal powders as the main raw materials.

The quality of the manufactured parts is greatly affected by the properties of powder material, such as surface quality and morphology [4–6]. Thus, accurately controlling the powder morphology is crucial to increasing the quality of MAM parts.

In general, the powder morphology is closely related to the production technique, which commonly includes gas atomization (GA) [7], plasma rotating electrode process [8], and plasma atomization [9]. Among them, the GA method is the

main production technique for fine spherical powders in MAM [10,11]. During the GA process, the metal melt is disintegrated into many spherical droplets by high-speed gas jets. The high cooling rate during the GA process (10⁵–10⁶ K/s) makes it possible to produce powders with reduced segregation [12]. Nevertheless, controlling powder defects has always been a critical issue for GA powders, e.g., hollow particles. The detailed physical behavior during the GA process is not completely understood.

Due to the complexity of the secondary atomization process (including droplet deformation and breakup, cooling, and solidification), it has a crucial influence on the properties of the prepared powders, especially the morphology [13]. For example, the formation of hollow particles is mainly related to the deformation and breakup of metallic droplets [14]. Extensive studies have been focused on the prediction of physical processes during secondary atomization recently [15–17]. These investigations revealed the flow physics and droplet dynamics that contributed to droplet breakup. In addition, some researchers have also conducted dimensionless analysis on secondary atomized droplet breakup to predict the powder particle size [18]. Several other researchers have performed in-situ observations of the droplet breakup process using high-speed cameras. They analyzed the effects of relevant dimensionless parameters (e.g., Weber number, Reynolds number) on the droplet breakup morphology and physical mechanisms [19,20]. Although the prediction of the secondary breakup process of metallic droplets has been extensively investigated, the droplet breakup characteristics have rarely been correlated with the morphology of the final powder particles, particularly with the hollow particle formation and evolution.

In this work, the relationship between the metallic droplet deformation and breakup behaviors and typical powder morphology was analyzed by experiments and numerical simulations. In addition, the influences of droplet temperature and gas velocity on the metallic droplet deformation and breakup behaviors and thus on the powder morphology were discussed in terms of the specific solidification characteristics of metallic droplets. The hollow particle formation mechanism and inhibition methods were also discussed in detail.

2 Experiment and simulation method

2.1 Materials and experiments

The pre-alloyed powder was produced using a vacuum induction melting gas atomization (VIGA) process with argon as the atomizing gas. The gas atomization experiments were carried out at a melt temperature of 1908 K and an atomizing gas pressure of 4 MPa. The melting crucible had a power of 150 kW and a refining time of 20 min. The insulation crucible had a power of 15 kW and an insulation time of 30 min. At the onset of the gas atomization process, the atomization chamber was vacuumed to 0-2 kPa, and then the smelting chamber was pressurized to 13-15 kPa. General results from the numerical simulations relating secondary breakup to the particle morphology using different droplet temperatures and gas velocities were validated by gas atomization experiments based on 316L stainless steel.

During gas atomization, the 316L melting temperature was measured by an infrared thermometer. Metallic powder samples were obtained using the three-point quadrature method, and their morphology was observed using a scanning electron microscope (SEM, Phenom XL G2) in secondary electron (SE) imaging mode at 15 kV. To observe the hollow particle section, the metal powders were mounted into a conductive resin and ground with SiC sandpapers from 2000 to 3000 grit. Then, the metal powders were sequentially finely polished with 2.5 and 0.5 µm diamond suspensions. Additionally, an I-SPEED 7 high-speed camera (using an AF 80-200 mm f/2.8D zoom lens) was utilized to record the gas atomization process. The primary atomization process was detected by the high-speed camera, but the secondary breakup behavior was difficult to observe due to the limited magnification of the camera lens. Therefore, numerical simulations were utilized to study the droplet breakup processes.

2.2 Model description and case setup

Secondary atomization is a complex physical process that involves high temperatures and high speeds, in which droplets deform or collide with each other [21]. This makes it difficult to describe the detailed droplet breakup behaviors in the whole

atomization chamber (macro-scale) due to the limited computational resources [22]. Because droplet breakup occurs randomly during gas atomization, only qualitative analysis of the association between droplet breakup and particle morphology was possible. Thus, the simulation model was simplified, and some assumptions were made:

- (1) The initial droplets were all spherical.
- (2) The initial temperature inside the particles was uniform, and the temperature only changed along the radial direction.
- (3) The initial velocity of secondary atomized droplets was 0, and the initial gas-liquid relative velocity was equal to the gas velocity. Within the computational domain, the relative gas velocity was assumed to be uniform and unidirectional.
- (4) The metallic droplet viscosity was described as a function of temperature.

Figure 1(a) shows high-speed camera photos of the primary atomization of the melt and the secondary atomization of the droplets during the VIGA process. To construct a correlation between gas atomization and child droplet breakup model, an investigation was conducted on the single-phase gas flow field of the close-coupled nozzle. The primary atomization simulation results were applied

as the initial conditions for droplet breakup, where the argon inlet pressure was P=4 MPa and 316L melting temperature was 1908 K. The droplet diameter (d) in the primary atomization simulation was measured using Image-Pro Plus software as \sim 750 µm, as shown in Fig. 1(b). The gas velocity was derived from the single-phase flow field simulation results of the close-coupled nozzle, as illustrated in Fig. 1(c). The initial gas velocity (u_g) was set using a gradient of 400, 300, 200, and 100 m/s according to the secondary atomization zone described by WEI et al [23]. Secondary atomization involves the deformation and breakup of solidifying droplets [24]. Hence, the initial droplet temperature (T_d) was set in a stepwise manner to 1650, 1608, or 1550 versus 1508 K, which was lower than the liquidus temperature. According to the findings of RIDOLFI and FOLGARAIT [18] on secondary atomization, where droplet breakup during gas atomization was primarily driven by top-downward gas flow, a single child droplet was extracted to build a cylindrical geometric simulation model, illustrated in Fig. 1(d). Accordingly, cases were set up to investigate the influence of initial droplet temperature and gas velocity on the droplet breakup characteristics, as listed in Table 1.

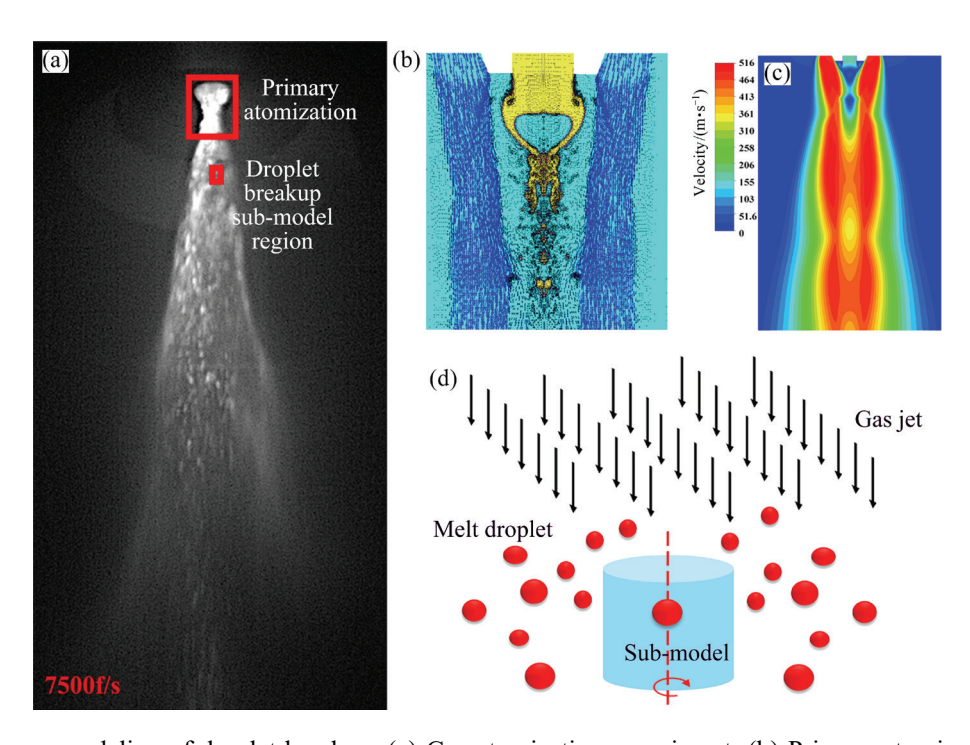


Fig. 1 Sub-process modeling of droplet breakup: (a) Gas atomization experiment; (b) Primary atomization simulation with close-coupled nozzle; (c) Single-phase gas flow field with close-coupled nozzle; (d) Sub-process model for droplet breakup

Table 1 Cases for numerical simulations

Case No.	Gas temperature/ K	Droplet diameter/ µm	Gas velocity/ (m·s ⁻¹)	Droplet temperature/ K
1	300	750	400	1650, 1608, 1550, 1508
2	300	750	400, 300, 200, 100	1650

2.3 Governing equations

The VOF method, coupled with the $k-\omega$ SST turbulence model, was employed to simulate metallic droplet deformation and breakup, which has been validated as suitable for droplet breakup simulations by RIDOLFI and FOLGARAIT [18]. In the VOF method, the droplet deformation and breakup processes are described by solving a set of momentum equations and tracking the volume fraction of each fluid in the entire region. The transport equation of the volume fraction in the VOF method is expressed as follows [22,25]:

$$\frac{1}{\rho_{q}} \left[\frac{\partial}{\partial t} (\alpha_{q} \rho_{q}) + \nabla \cdot (\alpha_{q} \rho_{q} \mathbf{u}_{q}) = S_{\alpha_{q}} \right]$$
 (1)

where α is the volume fraction, ρ is the mass density, \mathbf{u} is the velocity, q represents the q phase, and S_{α_q} is the source term. In the droplet breakup simulation, gas was set as the primary phase and metallic droplets as the secondary phase. However, the transport equation of the volume fraction will be solved, not directly for the primary phase. The transport equation of the volume fraction of the primary phase is restricted according to the following conditions:

$$\sum_{q=1}^{n} \alpha_q = 1 \tag{2}$$

Momentum equation is [23]

$$\frac{\partial}{\partial t}(\rho \mathbf{u}) + \nabla \cdot (\rho \mathbf{u} \mathbf{u}) + \nabla P = \nabla \cdot \left[\mu (\nabla \mathbf{u} + \nabla \mathbf{u}^{\mathrm{T}})\right] +$$

$$\rho \mathbf{g} + \mathbf{F} + \frac{(1-\beta)^2}{\beta^3 + \varepsilon} A(\mathbf{u}_1 - \mathbf{u}_p)$$
 (3)

where $\nabla \boldsymbol{u}^{\mathrm{T}}$ is the velocity transpose matrix, ΔP is the pressure difference, \boldsymbol{g} is gravitational acceleration, \boldsymbol{F} is the body force, β is the liquid volume fraction, ε is a constant (<0.0001), \boldsymbol{u}_1 is the liquid phase velocity, and $\boldsymbol{u}_{\mathrm{p}}$ is the solid velocity due to the pulling-out of solidified material from

the domain. A is the mushy zone constant, which measures the amplitude of damping; the higher this value, the steeper the velocity gradient of the material to zero as it solidifies.

Metallic droplet deformation and breakup are usually accompanied by droplet cooling and solidification processes. The droplet energy equation is as follows [26]:

$$\frac{\partial}{\partial t}(\rho H) + \nabla \cdot (\rho \mathbf{u} H) = \nabla \cdot (k\Delta T) + S \tag{4}$$

The enthalpy of the material (H) is calculated as

$$H=h+\beta L$$
 (5)

where $h(=h_{ref} + \int_{T_{ref}}^{T} c_p dT)$ is the sensible enthalpy, h_{ref} is the reference enthalpy, T_{ref} is the reference temperature, c_p is the specific heat at a constant pressure, L is the latent heat, and k is the heat

The definition of liquid volume fraction (β) can be written as

transfer coefficient.

$$\begin{cases} \beta = 0 \ (T < T_{\text{solidus}}) \\ \beta = 1 \ (T > T_{\text{liquidus}}) \\ \beta = \frac{T - T_{\text{solidus}}}{T_{\text{liquidus}} - T_{\text{solidus}}} \ (T_{\text{solidus}} \le T \le T_{\text{liquidus}}) \end{cases}$$

$$(6)$$

where T_{solidus} is the solidus temperature, and T_{liquidus} is the liquidus temperature.

During the secondary atomization process, the droplet breakup is mainly affected by aerodynamic forces, viscous forces, and surface tension forces. Two important dimensionless parameters are thus proposed to characterize the droplet fragmentation behavior, i.e., Weber number (*We*) and Ohnesorge number (*Oh*) [27]:

$$We = \frac{\rho_{\rm g} u_{\rm rel}^2 d}{\sigma} \,, \quad Oh = \frac{u_{\rm d}}{\sqrt{\rho_{\rm d} d\sigma}} \tag{7}$$

where $\rho_{\rm g}$ and $\rho_{\rm d}$ are the mass density of gas and droplet, respectively, $u_{\rm rel}$ is the relative velocity of the gas jet to the atomized droplet, d is the initial diameter of the metallic droplet, $u_{\rm d}$ is the droplet viscosity, and σ is the surface tension. A larger We indicates a larger aerodynamic force during destruction, and thus a larger tendency for droplets to break up. On the other hand, a larger Oh indicates a larger droplet viscous force, and thus a

lower tendency for droplets to break up. Generally, droplet breakup in the fully-liquid state is mainly related to *We*. Table 2 lists different droplet breakup modes in different droplet *We* ranges. Based on this, the droplet was theoretically broken via shear breakup in Case 1 when the initial droplet temperature was 1650, 1608, 1550, and 1508 K. However, when the atomizing gas velocity was increased from 100 to 400 m/s in Case 2, the droplet may have undergone no breakup, bag breakup, multimode breakup, or shear breakup, as shown in Fig. 2.

Table 2 Different *We* ranges corresponding to different droplet breakup modes [28]

Breakup mode	We range
Vibrational (no breakup)	0-11
Bag	11-35
Multimode	35-80
Shear	80-350

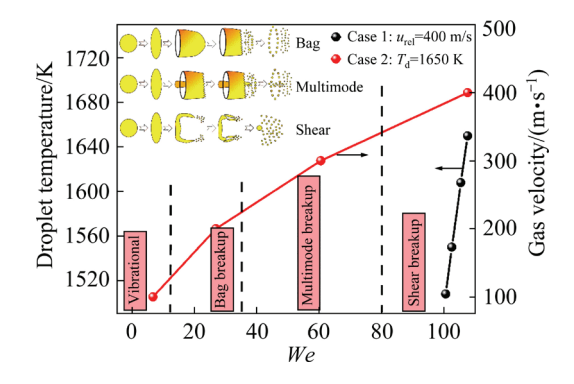


Fig. 2 We distribution of initial metallic droplet

2.4 Boundary condition settings and numerical procedure

To match available computational resources, the cylindrical geometric model of the simulation was simplified into a 2D axisymmetric geometry, as shown in Fig. 3. In setting the boundary conditions for droplet breakup simulations, the top of the computational domain was defined as the gas velocity inlet boundary where the velocities were set to be 100, 200, 300, or 400 m/s, and the inlet gas temperature was set to be 300 K. The bottom was defined as the pressure outlet boundary because the bottom of the computational domain was the actual spatial position in the atomization chamber, where the pressure and temperature were set to be 0 kPa and 300 K, respectively. At the inlet and outlet

boundaries, the turbulent intensity was defined and evaluated in terms of the Reynolds number (Re) using the equation $I=0.16Re^{-1/8}$. Because the selected cylindrical area containing a droplet was small, it was assumed that there was no velocity gradient between the side of the cylindrical area and the exterior of computational domain. Therefore, the left side of the computational domain was defined as the stationary wall boundary. The right side was set as the axis boundary because Fluent software required the axis of symmetry to be parallel to the x-axis. The default property data of argon in Fluent 19.2 were used in this work. As listed in Table 3, the main thermodynamic parameters of 316L stainless steel during droplet disintegration simulations were taken from the literature. Variations in the physical properties of materials with temperature were defined by the piecewise function in the material definition section of ANSYS FLUENT 19.2. The initial droplet diameter d, temperature T_d , and velocity u_d were added by patches, where $d=750 \mu m$, $T_d=1650$, 1608, 1550, or 1508 K, and $u_d=0$ m/s. In addition, the computational domain was divided into quadrilateral structural grids using ICEM for an initial cell number of 198801 and an initial minimum cell size of 17 μm.

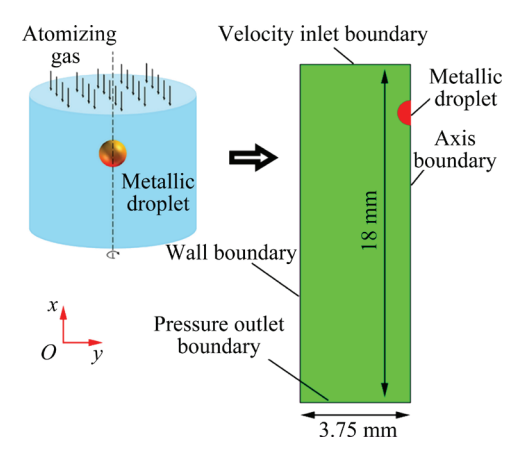


Fig. 3 Computational domain and boundary conditions

An unsteady solver was employed and resolved using the ANSYS Fluent 19.2 code for the droplet breakup process. The solution was based on the coupled algorithm, which computes discrete mathematical models with coupled pressure and velocity. Density, momentum, and energy were formulated in the first-order upwind style scheme. The compressive scheme and the PRESTO! method were used for volume fraction and pressure

interpolation, respectively. The transient calculation time step for droplet breakup simulation was 2×10^{-8} s. The flow Courant number (*Co*) was defined below 0.2 to ensure computational stability. To capture more details about droplet breakup, the volume fraction gradient was used to adaptively refine the mesh around the interface. The maximum refinement level of the mesh was level 2, and the minimum mesh size after refinement was 5 μ m. The criteria of convergence were that the residual values were less than 1×10^{-3} for the continuity/momentum equations and 1×10^{-6} for the energy equation, respectively.

Table 3 Physical parameters of 316L stainless steel melt [29]

men [27]		
Parameter	Value	
Density/(kg·m ⁻³)	7050 (1708 K), 7220 (1658 K), 7300 (1568 K), 7350 (1493 K), 7660 (793 K), 7850 (298 K)	
Solidus temperature/K	1493	
Liquidus temperature/K	1708	
Latent heat of melting/(J·kg ⁻¹)	2.7×10 ⁵	
Specific heat capacity/ $(J \cdot kg^{-1} \cdot K^{-1})$	755 (1600 K), 502 (298 K)	
Surface tension coefficient/ $(N \cdot m^{-1})$	3.28-0.00089 <i>T</i>	
Thermal conductivity/ $(W\!\cdot\! m^{-1}\!\cdot\! K^{-1})$	29.99 (1708 K), 32.56 (1668 K), 32.49 (1618 K), 31.12 (1493 K), 15.76 (298 K)	
Viscosity/(Pa·s)	$10^{2358.2/T-3.5958}$ ($T > 1493$ K), 6+ $(1493-T) \times 0.01$ ($T \le 1493$ K)	

T is the temperature in K

2.5 Model validation

The grid independence for droplet breakup simulation was analyzed (d=0.75 mm, T_d =1650 K, u_g =400 m/s, and t=60 μ s). The effect of mesh density on the maximum diameter of a circular liquid film was discussed for five sets of different meshes in the droplet breakup simulation. As shown in Fig. 4, when the cell number was larger than 198801 in the droplet breakup simulation, the relative error of the maximum diameter of the circular liquid film was less than 1.8%. Therefore, a cell number of 198801 was adopted in subsequent simulations to obtain a balance between accuracy and computational costs.

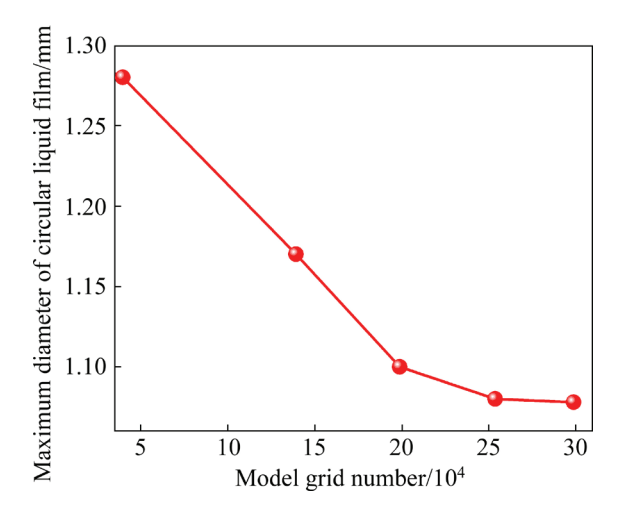


Fig. 4 Grid independence analysis

In this work, no experiments were carried out to directly capture the details of the breakup process of metallic droplets during the GA process. In this case, a theoretical model developed by HU et al [30] was adopted to verify the credibility of the present numerical simulation method and its results. The model was built for an FeNiCrBSiC alloy and ignored the effects of droplet breakup and collisions. The nucleation and cooling solidification model were applied with convection as the dominant cooling approach. In their work, the relationship between average cooling rate and droplet size was determined from measured data and empirical formula as follows:

$$\chi = \left(\frac{40}{0.3908 + 0.00756 d}\right)^3 \tag{8}$$

where γ is the average cooling rate. The model was built based on an atomizing gas velocity of u_g =450 m/s and an initial melt droplet temperature of T_d=1848 K. The applicability of the theoretical model was verified. Figure 5(a) depicts comparison of the average cooling rate curves between the theoretical estimation data and the numerical simulation results. To ensure consistency with the modeling assumptions by HU et al [30], the averaged cooling rates computed from the numerical simulations only accounted for the earlier stages when the droplets were unbroken ($t=20 \mu s$). As shown in Fig. 5(a), the simulated average cooling rates were 105631, 68840, 44920, 30546 and 22886 K/s, and the theoretically estimated data were 106300, 64852, 42434, 29265 and 21028 K/s when the droplet diameters were 60, 80, 100, 120,

and 140 μ m, respectively. The maximum error of 8.8% occurred when d=140 μ m. Therefore, the present numerical model can reasonably predict droplet cooling behavior during the droplet breakup.

Figure 5(b) illustrates non-dimensional droplet deformation, which was defined to depict the droplet deformation in terms of the ratio of the characteristic length (d_1) of the deformed droplet to the initial droplet diameter (d_0) , as described by STEFANITSIS et al [15]. For consistency and comparability to previous literature, characteristic transport time t was normalized to obtain dimensionless time τ :

$$\tau = t \frac{u_{\rm g}}{d_0} \sqrt{\frac{\rho_{\rm g}}{\rho_{\rm d}}} \tag{9}$$

To validate the simulation method and its results, a Galinstan droplet model for air atomization using We=13.2, $u_g=74.6$ m/s, $u_d=0$ m/s, and $d_0=1.32$ mm was built to compare with the experimental

non-dimensional droplet deformation results of HOPFES et al [20]. As the dimensionless time τ increased, the simulated and experimental nondimensional droplet deformations were 1.00, 1.13, 1.38, 1.72, 2.01, 2.25, 2.47, 2.89, 3.32, 4.33, and $1.00(\pm 0)$, $1.05(\pm 0)$, $1.30(\pm 0.011)$, $1.56(\pm 0.031)$, $1.89(\pm 0.022)$, $2.07(\pm 0.052)$, $2.36(\pm0.036)$, $3.03(\pm 0.038)$, and $4.11(\pm 0.063)$, $2.68(\pm0.038)$, respectively. There was good agreement between the experimental and simulated values, and the maximum error of the simulation was 9.4% when τ =1.5. Therefore, the current model can reasonably predict the deformation process of melt droplets.

3 Results

3.1 Gas-droplet interaction mechanisms

Figure 6(a) illustrates the gas velocity field of the gas—droplet atomization procedure, which reveals the deformation and breakup behavior of the droplet. Interactions between the incident gas flow

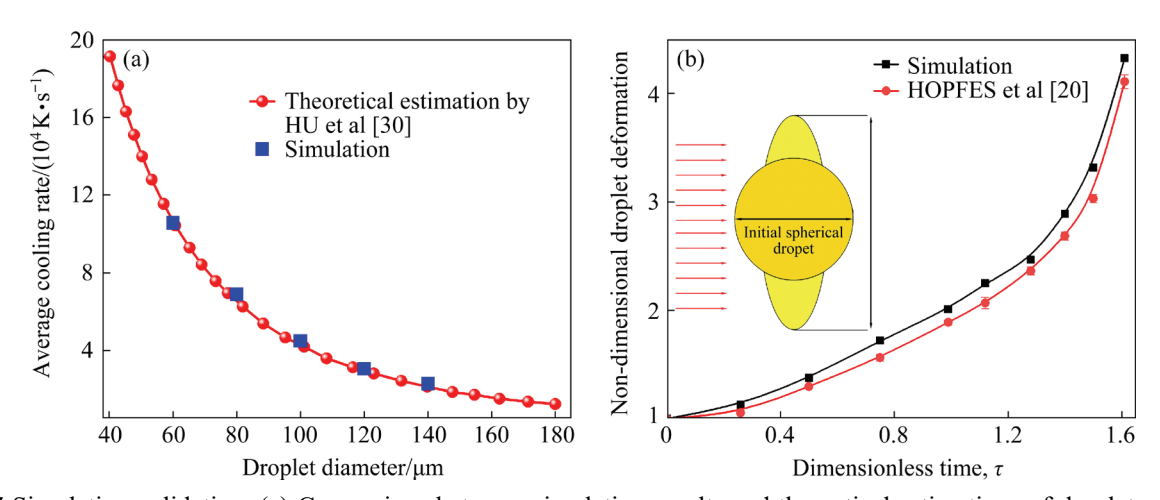


Fig. 5 Simulation validation: (a) Comparison between simulation results and theoretical estimations of droplet average cooling rate; (b) Comparison of simulation results with non-dimensional droplet deformation from experimental data of HOPFES et al [20]

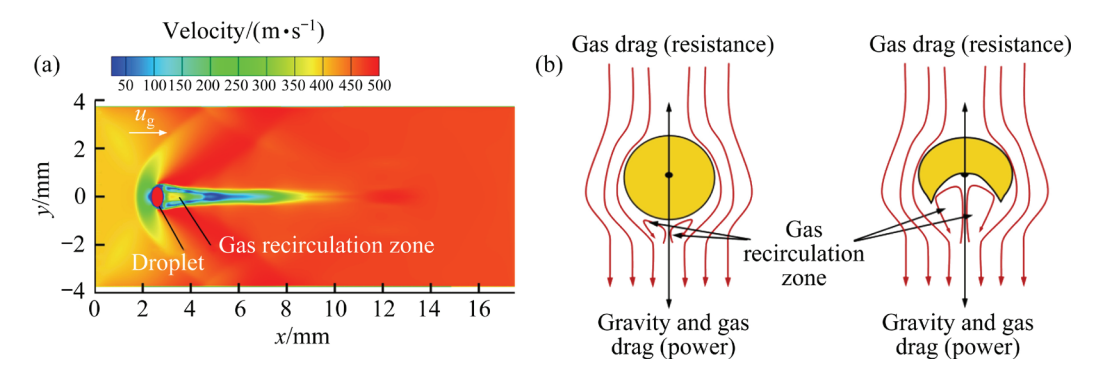


Fig. 6 (a) Gas velocity field distribution when $u_g=400 \text{ m/s}$; (b) Schematic diagram of forces on droplet

and the droplet surface changed the gas flow conditions surrounding the droplet, which formed a high-pressure gas recirculation zone at the bottom of the droplet. A reflected wave was formed on the top of the droplet [31], which reduced the gas velocity within the region, whereas the gas velocity around the side of the droplet was increased.

During a droplet's flight, it is mainly affected by the gravitational force and gas drag (power and resistance), as shown in Fig. 6(b). The effect of the high-pressure gas recirculation zone on the bottom of the droplet caused the droplet to form a circular liquid film due to a pressure difference between its front and back surfaces [32], which indicates the beginning of the breakup process.

3.2 Effects of droplet temperature on droplet breakup

Figure 7 compares the characteristics of the metallic droplet deformation process during atomization secondary at different droplet temperatures. Figure 7(a) depicts that when the initial temperature of the droplet was 1650 K, it began to deform at 10 µs, while the shear breakup of the droplet occurred at 40 µs. However, it can be seen from Fig. 7(b) that when the droplet temperature was reduced to 1608 K, the droplet began to deform slightly at 20 µs. Finally, multimode droplet breakup occurred from 80 to 100 µs. The bag and liquid core were formed during breakup. Figure 7(c) depicts that when the initial temperature of the droplet was further reduced to 1550 K, the droplet just started to distort at 20–40 µs interval. As a result, at 100 µs, the droplet gradually disintegrated in a form similar to the bag breakup mode, forming an open bag liquid film. Finally, when the droplet temperature was lowered to 1508 K, the final droplet deformation degree was smaller than that of the previous cases, and a curved droplet and very few children droplets were formed, as shown in Fig. 7(d).

Figure 8 illustrates temporal variations in the vertex average temperature (VAT) of metallic droplets with different initial temperatures during droplet deformation and breakup. Figure 8(a) demonstrates the temporal VAT variation within the droplet (the region of liquid volume fraction \geq 90%), which indicated that the droplet cooling rate rose gradually and was higher in the droplet breakup stage than in the deformation stage. For example, for the droplet with an initial temperature of T_d =1650 K, the average cooling rate of the droplet during the deformation stage (10–40 μ s) was 75000 K/s, whereas the cooling rate during the breakup stage (40–100 μ s) was 183333 K/s. This was attributed to the increased surface area during

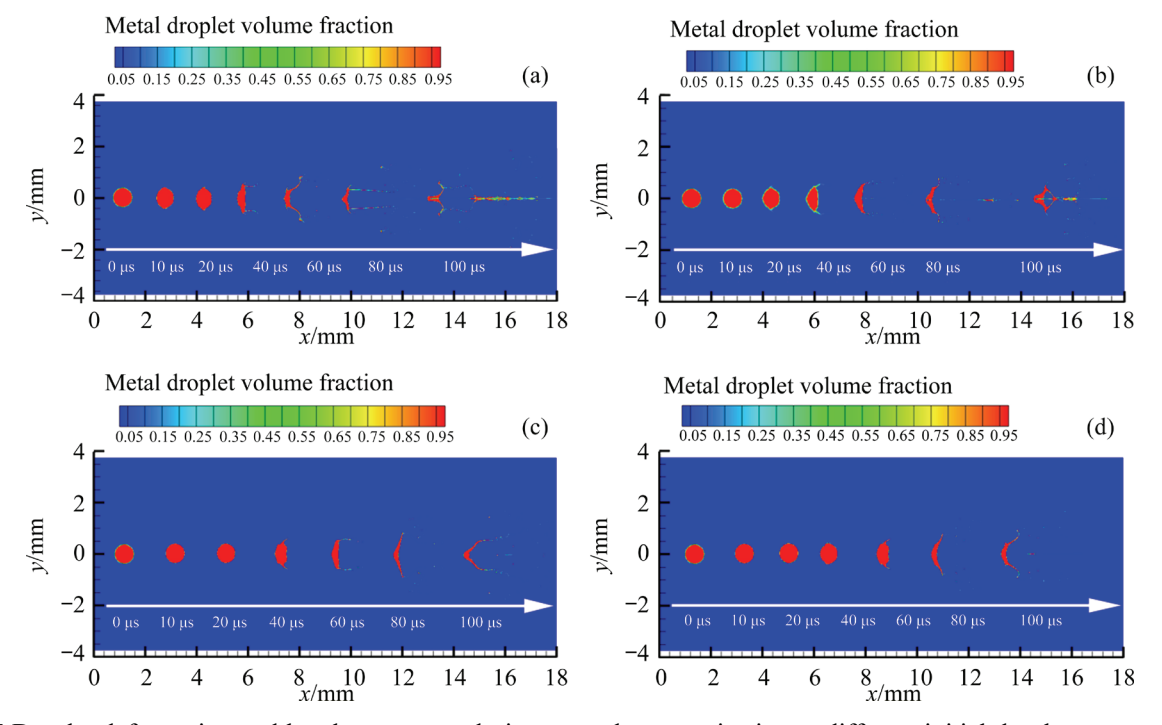


Fig. 7 Droplet deformation and breakup process during secondary atomization at different initial droplet temperatures: (a) 1650 K; (b) 1608 K; (c) 1550 K; (d) 1508 K

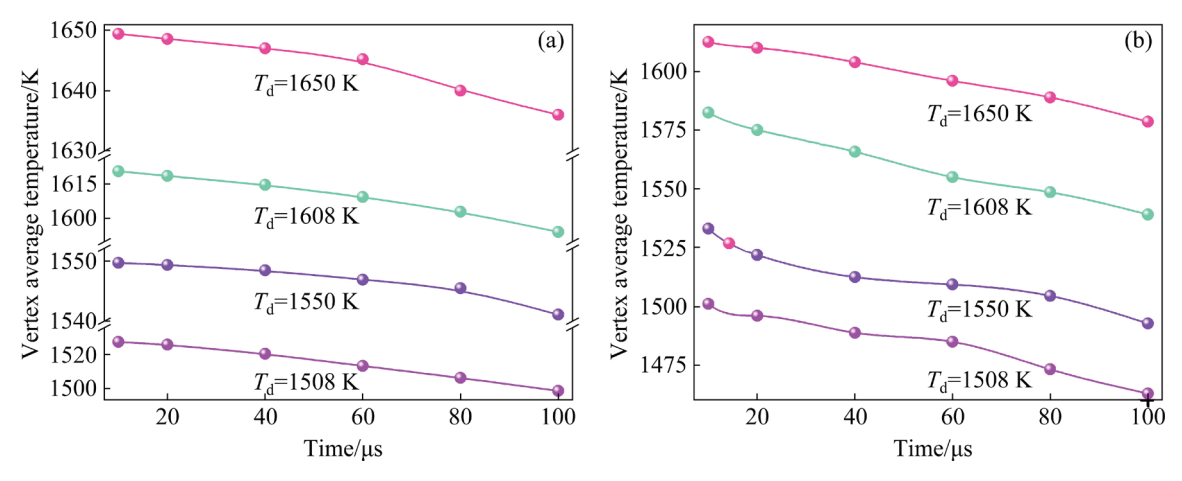


Fig. 8 Vertex average temperature distribution during droplet deformation and breakup process with different initial droplet temperatures: (a) Within droplets; (b) At droplet–gas interface

the droplet breakup stage. In addition, a very large temperature gradient existed around the droplet—gas interface, which contributed to the lowest temperature at the droplet surface. The VAT around the droplet—gas interface was thereby extracted from regions where the liquid volume fraction was between 1% and 90%, as indicated in Fig. 8(b). During the droplet deformation and breakup process (time period: $10-100~\mu s$), the VAT of the droplet—gas interface decreased from 1613 to 1580 K for the case where T_d =1650 K, from 1583 to 1539 K for T_d =1608 K, from 1533 to 1493 K for T_d =1508 K.

The viscous force F_z of the melt liquid was defined by [33]

$$F_z = \frac{16\,\sigma}{15} \sqrt{\frac{m}{k_{\rm B}T}} \frac{\mathrm{d}u}{\mathrm{d}z} \tag{10}$$

where m is the atomic mass, $k_{\rm B}$ is the Boltzmann constant, T is the melt liquid temperature, and du/dz is the shear rate. Therefore, the viscous force usually rises upon decreasing the droplet temperature. During droplet breakup, the internal temperature of a droplet decreases, increasing the viscous force, especially for the droplets with a lower initial temperature. However, variations in the viscous force within the droplet may not be significant due to the smaller VAT decrease. For example, for the case in which $T_{\rm d}$ =1550 K, the VAT of the droplet decreased from 1550 to 1541 K only. In contrast, the VAT of the droplet–gas interface was significantly lower, particularly for cases of $T_{\rm d}$ =1550 K and $T_{\rm d}$ =1508 K, where the final

temperature was close to or less than the solidus temperature. Therefore, the viscous force decreased from the droplet surface to the interior, and this effect became more obvious as the initial droplet temperature decreased. This means that the initial droplet temperature affects the droplet deformation period and the predetermined breakup mode (Figs. 2 and 7), which is consistent with the conclusions of WANG et al [34].

The droplet solidification process during secondary atomization was analyzed by varying the initial droplet temperature, as shown in Fig. 9. When the initial droplet temperature was 1650 K, the simulation results revealed that the droplet had a volume fraction of the liquid phase of about 73% due to the higher droplet temperature. This indicated that the droplet quickly completed the shear breakup process, as shown in Fig. 9(a). When the droplet temperature was reduced to 1608 K, 53% of the droplet was initially solidified, as shown in Fig. 9(b), demonstrating that the viscous resistance was relatively large. As a result, the time to initiate droplet deformation was 10 µs slower compared with the former due to the increased viscous force. The droplet breakup mode also changed from shear breakup at 10-60 µs to multimode breakup at 60–100 μs. When the initial temperature was lowered to 1550 K, the volume fraction of the liquid phase in the droplet was only 26.5%, as shown in Fig. 9(c). The viscous force during droplet deformation, in this case, was larger than that in the first two cases, resulting in the final droplet disintegration in a bag breakup manner since a deeper open bag film was formed at 100 µs.

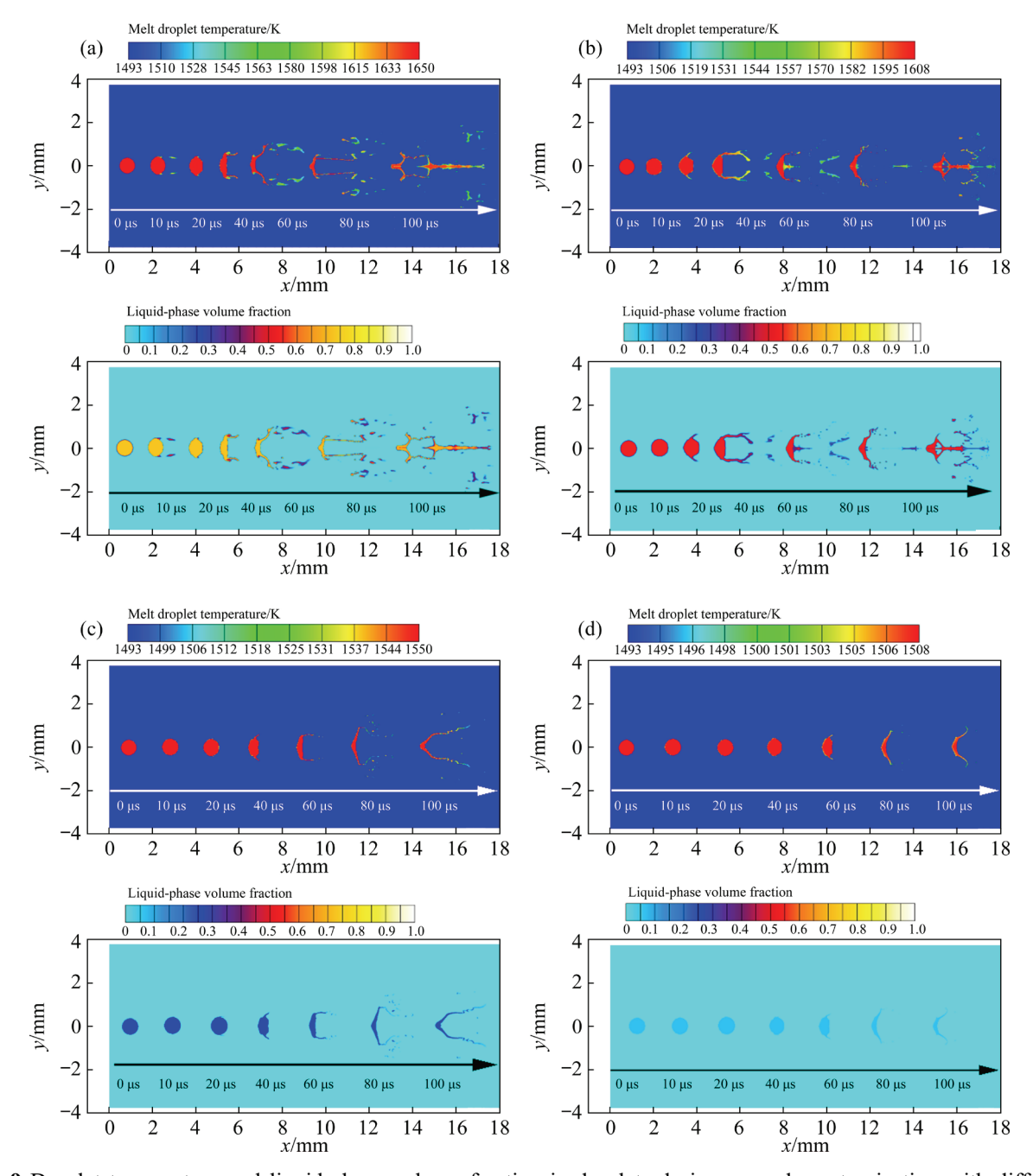


Fig. 9 Droplet temperature and liquid-phase volume fraction in droplets during secondary atomization with different initial droplet temperatures: (a) 1650 K; (b) 1608 K; (c) 1550 K; (d) 1508 K

The droplet breakup mode changed from shear breakup $(0-80~\mu s)$ to bag breakup $(80-100~\mu s)$. Careful observations revealed that the tip of the deformed liquid film could no longer form a closed bag liquid film because the temperature remained in the range of 1525-1532~K, where there was a very small volume fraction (about 15%-18%) of the liquid phase in the droplet. Figure 9(d) illustrates that when the initial temperature of the droplet was 1508~K, the volume fraction of the liquid in the droplet was only about 7%. It is necessary to state

that the liquid droplets were basically solidified, so only droplet deformation occurred due to the relatively large viscous force.

Overall, the droplets during secondary atomization transformed the expected breakup mode or only underwent deformation due to the higher viscous force as the temperature of the droplets decreased. Therefore, distinct from conventional water droplets, predictions of metal droplet breakup modes should be based on a comprehensive evaluation of *We* and *Oh* during

the deformation-fragmentation process [35]. In addition, it is expected that the changes in the droplet breakup mode will affect the final powder morphology.

The SEM images in Fig. 10 exhibit the typical morphology (excluding satellite particles) of metallic powders prepared by gas atomization at a gas pressure of 4 MPa and a melt temperature of 1908 K. The images show the presence of spherical particles, closed hollow particles, incompletely spheroidized particles, open hollow particles, and curved particles. This helped establish a relationship between droplet breakup and powder morphology. The droplet breakup at an initial temperature of 1650 K mainly produced spherical particles because the child droplet temperature reached 1590 K, where the liquid phase accounted for about 45% (Fig. 9(a)), as demonstrated in Fig. 10(a). However, upon lowering the droplet temperature to 1608 K, closed hollow particles or incompletely spheroidized particles were formed because the droplets underwent multi-mode

breakup during secondary atomization, forming a bag structure with a long liquid core in the middle (Fig. 9(b)). The liquid phase in the droplet bag accounted for 40%-45%. This implies that if the bag did not break during the subsequent deformation process, it will further solidify to form a closed hollow particle, similar to the conclusion of RABIN et al [36], as shown in Fig. 10(b). Otherwise, incompletely-spheroidized particles were formed after the bag film broke up, as indicated in Fig. 10(c). Since the liquid phase accounted for a relatively low proportion, there was insufficient time for the child droplets to spheroidize. Additionally, droplets that broke up at 1550 K easily formed incompletely spheroidized particles and open hollow particles, as shown in Figs. 10(c, d). This was because the temperature at the tip of the open liquid film formed during the atomization process decreased to 1525 K, and only about 15% of the liquid phase was present (Fig. 9(c)). Finally, as the droplet temperature decreased to 1508 K, curved particles were easily

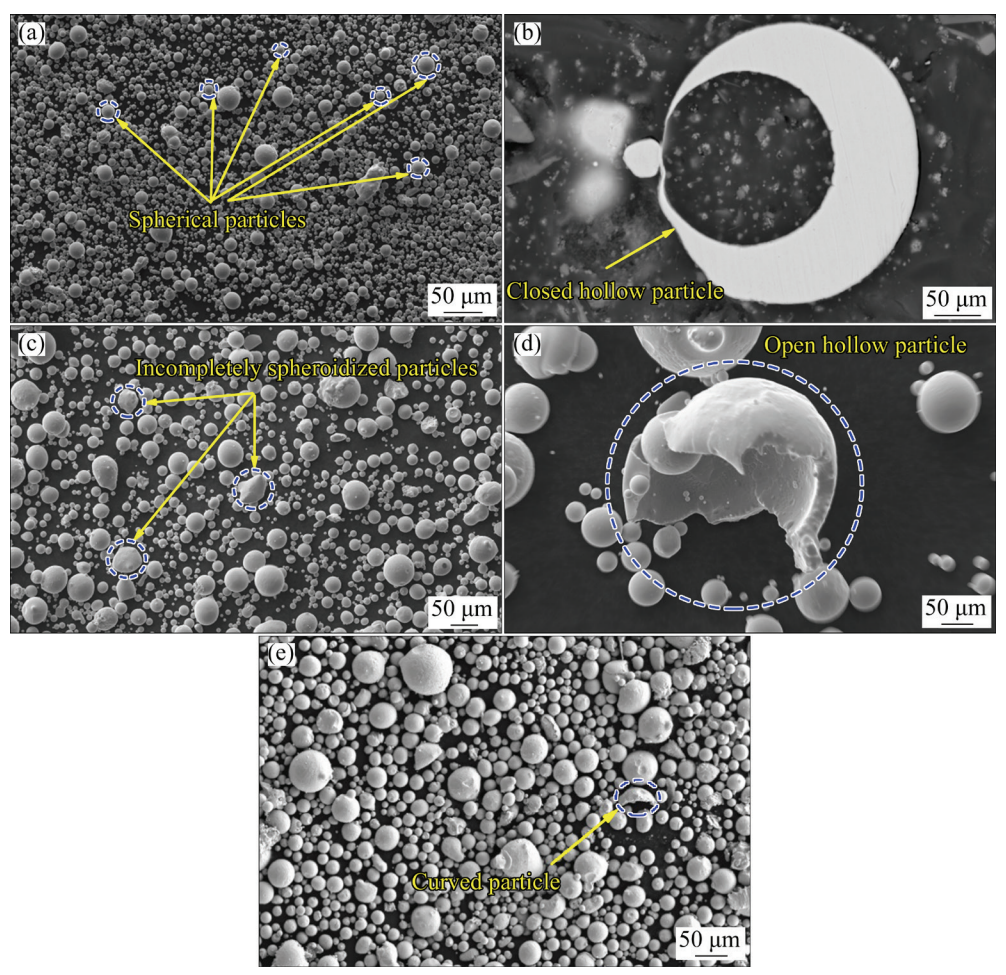


Fig. 10 SEM images showing different particle morphologies: (a) Spherical particles; (b) Closed hollow particles; (c) Incompletely spheroidized particles; (d) Open hollow particles; (e) Curved particles

formed because the droplet had limited curvature deformation (Fig. 9(d)), as shown in Fig. 10(e).

If the droplets undergo sufficient superheating, the child droplets will have enough time to spheroidize and solidify into spherical metallic particles. In summary, at a higher gas jet velocity, upon decreasing the initial temperature of the secondary atomized droplets, their tendency to form spherical particles gradually decreases. This may even lead to the formation of hollow particles, incompletely spheroidized particles, or curved particles. This is similar to the conclusions proposed by SEE and JOHNSTON [37], who declared that the droplet spheroidization time must be less than the solidification time to obtain spherical particles.

3.3 Effects of gas velocity on droplet breakup

Figure 11 displays the gas velocity distribution along the *x*-axis near the droplet with different inlet gas velocities, which reveals the aerodynamic behavior driving droplet deformation. In combination with the results in Section 3.1, the top gas velocity of the droplet decreased to zero due to the reflected wave effect. Additionally, a velocity peak appeared at the bottom of the droplet in the gas recirculation zone (Fig. 6(a)), where the peak velocity and width increased with the inlet gas velocity. The deformation of the droplet primarily

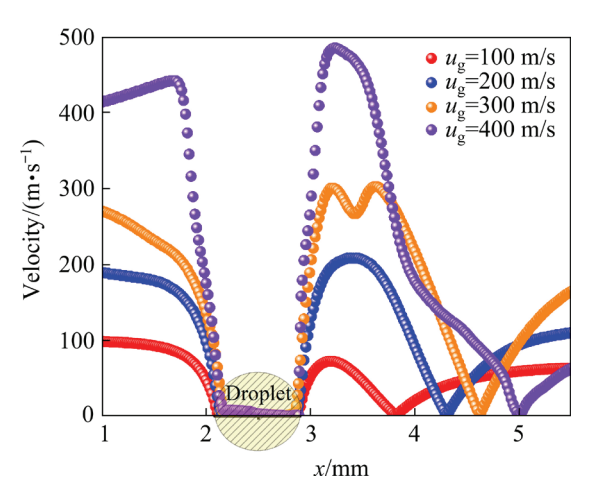


Fig. 11 Gas velocity distribution along *x*-axis near droplet

relied on the aerodynamic driving force between the top and bottom. It can be assumed that the droplet deformation driving force increased due to an increase in the inlet gas velocity.

Figure 12 displays the secondary atomization process of a single metallic droplet and illustrates the various breakup modes that are utilized to analyze the characteristics of film morphologies with different atomizing gas velocities. When the atomizing gas velocity was 400 m/s, the droplet began to deform at $10 \,\mu s$. Then, within the time period of $60{\text -}120 \,\mu s$, the droplet broke and deformed via shear breakup mode, as shown in

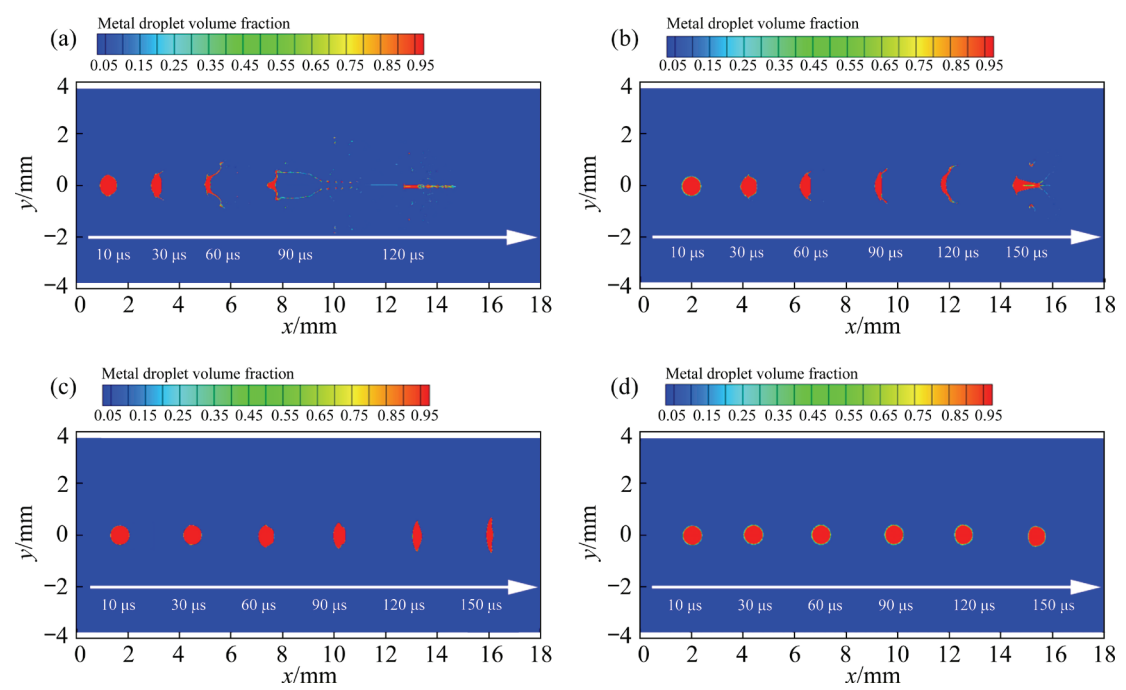


Fig. 12 Droplet deformation and breakup process during secondary atomization with different gas velocities: (a) 400 m/s; (b) 300 m/s; (c) 200 m/s; (d) 100 m/s

Fig. 12(a). When the gas velocity decreased to 300 m/s, the droplet began to deform at $30 \text{ }\mu\text{s}$. Secondary atomization of the droplet occurred via multi-mode breakup within the time period of $60-150 \text{ }\mu\text{s}$, as indicated in Fig. 12(b). When the gas velocity decreased to 200 m/s, the droplet began to deform at $60 \text{ }\mu\text{s}$. Then, within the period of $60-150 \text{ }\mu\text{s}$, the spherical droplet was unbroken but deformed into a sheet droplet, as indicated in Fig. 12(c). When the gas velocity decreased to 100 m/s, the droplets were slightly aspherical within the period of $10-150 \text{ }\mu\text{s}$ because the aerodynamic forces were too small (Fig. 12(d)).

Figure 13 illustrates the temporal variation of the vertex average temperature of the metallic droplets with different gas velocities during droplet deformation and breakup. Figure 13(a) demonstrates the temporal VAT variation within the droplet (the region of liquid volume fraction \geq 90%) with different gas velocities. When u_g =400 m/s, the VAT within the droplet decreased from 1649.4 to

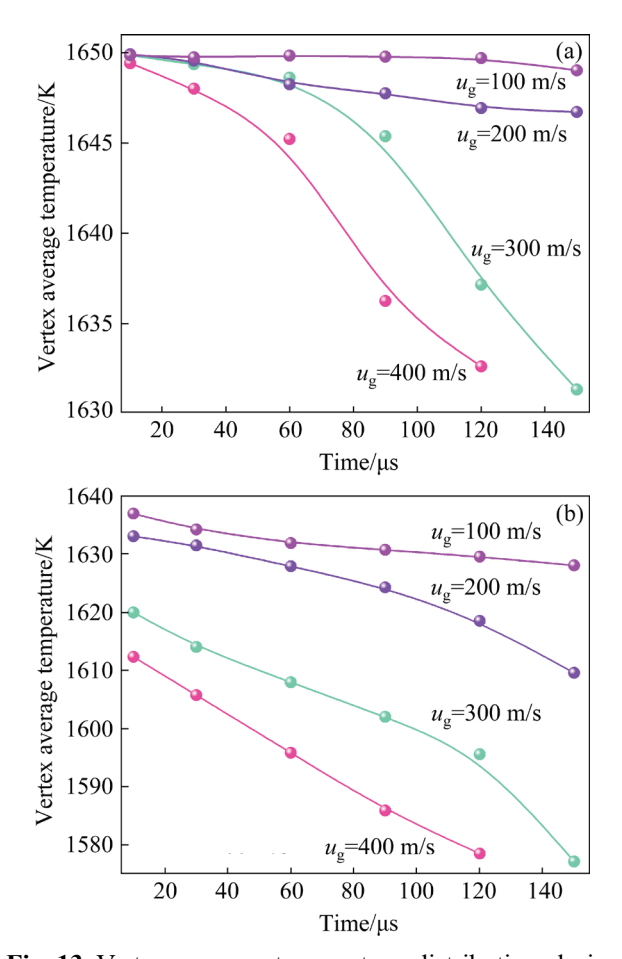


Fig. 13 Vertex average temperature distribution during droplet deformation and breakup process with different gas velocities: (a) Within droplets; (b) At droplet–gas interface

1632 K from 10 to 120 μs before complete breakup. When $u_g=300 \text{ m/s}$, the VAT within the droplet decreased from 1649.848 to 1631 K in an interval of 10–150 µs. The cooling rate of the droplet decreased greatly as the velocity of the atomizing gas decreased to or below 200 m/s. When u_g =200 m/s, the VAT within a droplet decreased from 1649.88 to 1646.698 K within an interval of 10–150 μ s. When u_g =100 m/s, the VAT within the droplet decreased slightly from 1649.89 to 1649.012 K within the interval of 10–150 μs. This indicates that the lower the gas velocity, the smaller the average cooling rate. The droplets were only deformed at $u_g=200 \text{ m/s}$ and $u_g=100 \text{ m/s}$ (Figs. 12(c, d)), resulting in a slower cooling rate. It should be mentioned that the temperature within the droplet varied only slightly during the droplet deformation and breakup process. However, the VAT near the droplet-gas interface (the region of liquid volume fraction between 1% and 90%) was noticeably lower, as illustrated in Fig. 13(b). The VAT around the droplet-gas interface was reduced to 1578.5 K for u_g =400 m/s (t=120 μ s), 1577.2 K for u_g =300 m/s (t=150 μ s), 1609.5 K for u_g =200 m/s (t=150 µs), and 1628 K for $u_g=100 \text{ m/s}$ (t=150 µs).

Based on the discussion in Section 3.2, the lower the temperature, the higher the viscous forces. Viscous forces may be significantly higher during the rapid cooling of droplets, especially near the gas-liquid interface, which affects droplet deformation and breakup. The effect of higher droplet viscous force can be weakened when the aerodynamic force dominates, e.g., for u_g =400 m/s and u_g =300 m/s. Thus, the results above show that the metallic droplet deformation starts earlier at higher gas velocities (Fig. 12). However, in the case of a weaker aerodynamic force, the increased droplet viscous force can hinder droplet breakup, thus changing the expected droplet breakup mode. For example, under the condition of u_g =200 m/s, the breakup mode changed from bag to vibrational breakup (Figs. 2 and 12(c)), which can be explained by the findings of HSIANG and FAETH [35].

Figure 14 illustrates the temperature and liquid-phase volume fraction in the droplet during secondary atomization, which exhibits the effect of gas velocity on the droplet breakup process to establish a correlation between gas velocity and the final powder morphology. As the gas velocity decreased from 400 to 100 m/s, the droplets

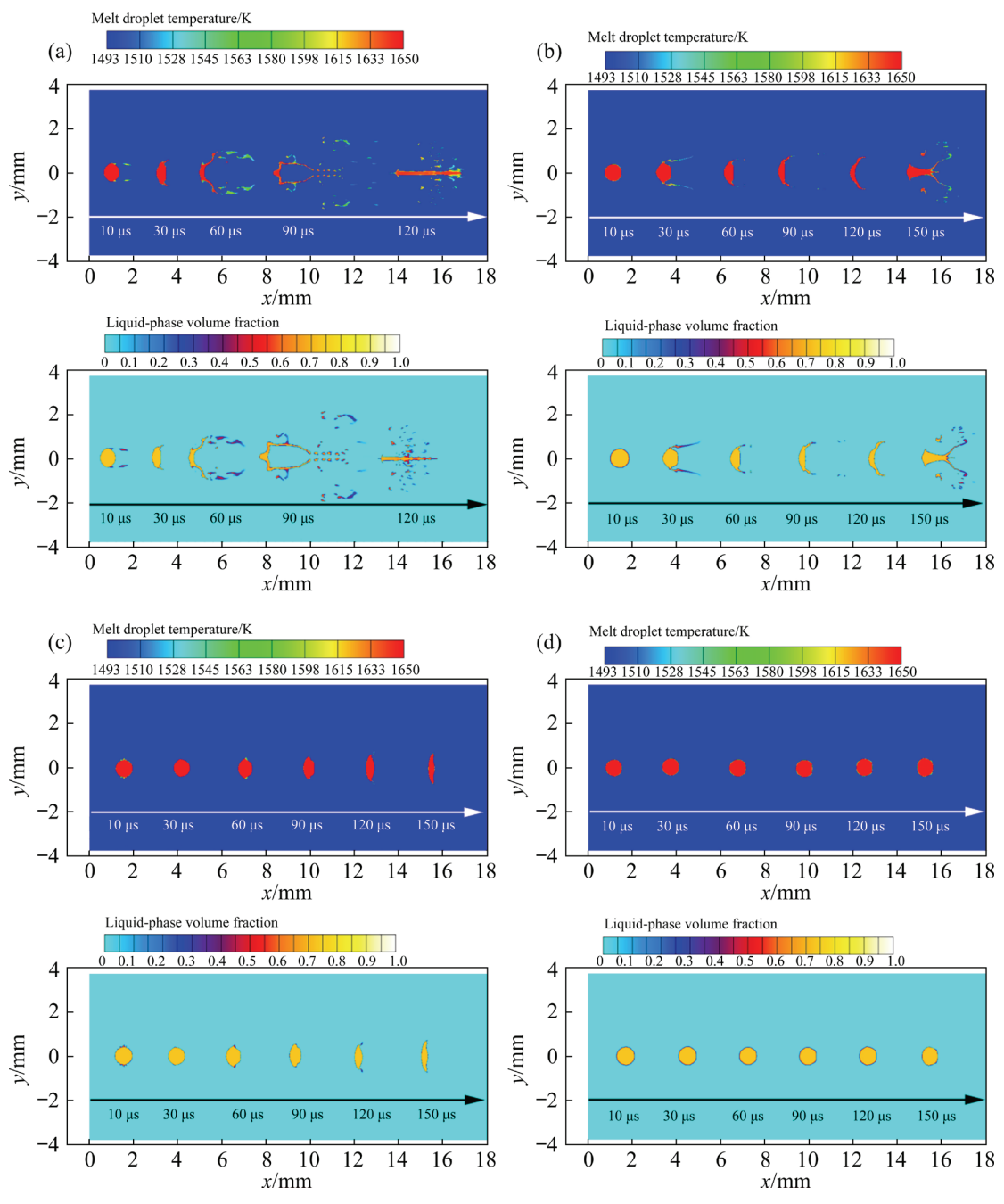


Fig. 14 Droplet temperature and liquid-phase volume fraction in droplets during secondary atomization with different gas velocities: (a) 400 m/s; (b) 300 m/s; (c) 200 m/s; (d) 100 m/s

underwent different types of breakup modes, including shear breakup, multi-mode breakup, bag breakup, and vibrational breakup (Fig. 2). The viscous force in the droplet increased during this process, especially at the droplet–gas interface (Fig. 13). This indicates that the spherical metallic particles were the primary products formed at a high gas velocity (e.g., u_g =400 m/s and u_g =300 m/s) because the temperature of the main part of droplet breakup remained at about 1645 K, where about

70% of the liquid phase was present. Only the edge of the liquid film or the child droplets had a lower liquid volume fraction (40%–60%), as demonstrated in Figs. 14(a, b) and Fig. 15(a), respectively. Here, the aerodynamic force was dominant over the viscous force. Nevertheless, when the gas velocity decreased to 200 m/s, sheet particles were formed because solidified sheet droplets could not be broken further, as shown in Figs. 14(c) and 15(b). In this case, the aerodynamic

forces were too small for the droplets to break up, even though the temperature of the droplet was about 1645 K (the volume fraction of liquid phase was about 70%). In addition, the effect of the increased viscous force due to the lower temperature cannot be ignored. When the gas velocity was further reduced to 100 m/s, a coarse spherical droplet was formed. In this case, the temperature of the droplet also remained at 1645 K, where about 70% of the liquid phase was also maintained. But the droplet failed to break up due to the too small aerodynamic force and the hindrance by the increased viscous force, as illustrated in Fig. 14(d). The spherical droplets tended to form coarse particles with small satellite particles due to the coarse droplet and fine particle collisions [38], as shown Fig. 15(c).

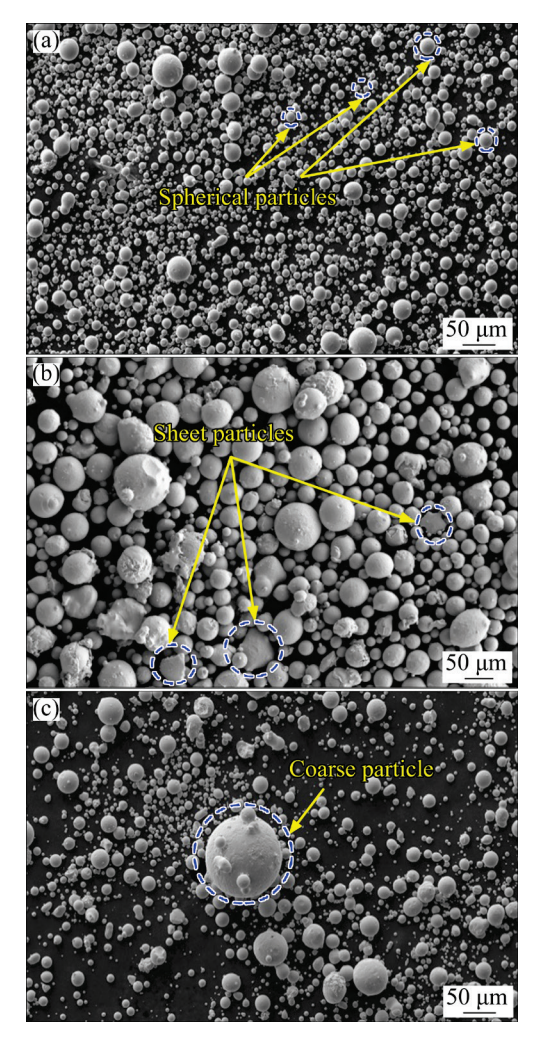


Fig. 15 SEM images of different particle morphologies produced from VIGA process at atomization pressure of 4 MPa and melt temperature of 1908 K: (a) Spherical particles; (b) Sheet particles; (c) Coarse particles

In general, at the same metallic droplet temperature (T_d =1650 K), the higher the gas velocity, the more likely it is to form spherical particles during secondary atomization. Otherwise, it is easy to produce sheet particles and satellite particles due to the insufficient aerodynamic force and the increased viscous force, which cannot be ignored. Thus, it is reasonable to assume that the small aerodynamic force and large viscous force increased the droplet deformation and spheroidization time, thus reducing the tendency towards spherical particle formation. This is consistent with the conclusions reported by SEE et al [37].

4 Discussion

4.1 Metallic droplet breakup behavior

Metallic droplet breakup is always a critical issue of gas atomization technologies [18,39], but detailed discussions on metallic droplet deformation and breakup have rarely been reported. During secondary atomization, the aerodynamic force deforms and fragments metallic droplets, while the viscous force acts as the primary resistance to droplet deformation [27]. As discussed in Section 3.1, the external forces imposed on a flying droplet are primarily the gas drag force (F_D) and gravitational (F_g) and the negligible buoyancy (F_f) forces, as follows [40]:

$$F_{\rm D} = 1/2C_{\rm d}\rho_{\rm g} \left(u_{\rm g} - u_{\rm d}\right) \left|u_{\rm g} - u_{\rm d}\right| A_{\rm d}$$
 (11)

$$F_{g} = \rho_{l} V_{d} g \tag{12}$$

$$F_{\rm f} = \rho_{\rm g} V_{\rm d} g \tag{13}$$

where C_d is the drag coefficient, A_d is the maximum cross-sectional area of the droplet, V_d is the droplet volume, and g is the magnitude of gravitational acceleration.

In this study, the effects of droplet temperature and gas velocity on the deformation and breakup behaviors of metallic droplets were discussed. These two variables mainly affect the droplet deformation resistance, i.e., the viscous force (Fig. 7) and the aerodynamic driving force (Eq. (11)). In theory, when the condition $F_D+F_g+F_z>0$ is met, a metallic droplet begins to deform. A droplet tends to breakup when the aerodynamic force dominates the viscous force; otherwise, a droplet tends to only deform [19]. Thus, to describe

the deformation and breakup behaviors of metallic droplets, the ratio of aerodynamic to viscous force (Φ) is introduced and defined as

$$\Phi = \lg\left(\frac{We}{Oh^2}\right) = \lg\left(\frac{\rho_g \rho_d u_{rel}^2 d^2}{u_d^2}\right)$$
 (14)

Figure 16 displays the temporal variation of Φ near the droplet–gas interface during droplet breakup at different initial droplet temperatures and gas velocities. In an interval of 10–100 µs, the Φ value decreased from 7.11 to 7.04 for the case T_d =1650 K, from 7.05 to 6.97 for T_d =1608 K, from 6.96 to 1.46 for T_d =1550 K, and from 6.9 to 1.41 for T_d =1508 K, as shown in Fig. 16(a). In addition, the Φ value decreased from 7.11 (t=10 µs) to 7.04 (t=120 µs) for the case u_g =400 m/s, from 6.87 (t=10 µs) to 6.79 (t=150 µs) for u_g =300 m/s, from 6.53 (t=10 µs) to 6.5 (t=150 µs) for t=200 m/s, and from 5.94 (t=10 µs) to 5.92 (t=150 µs) for t=100 m/s, as depicted in Fig. 16(b).

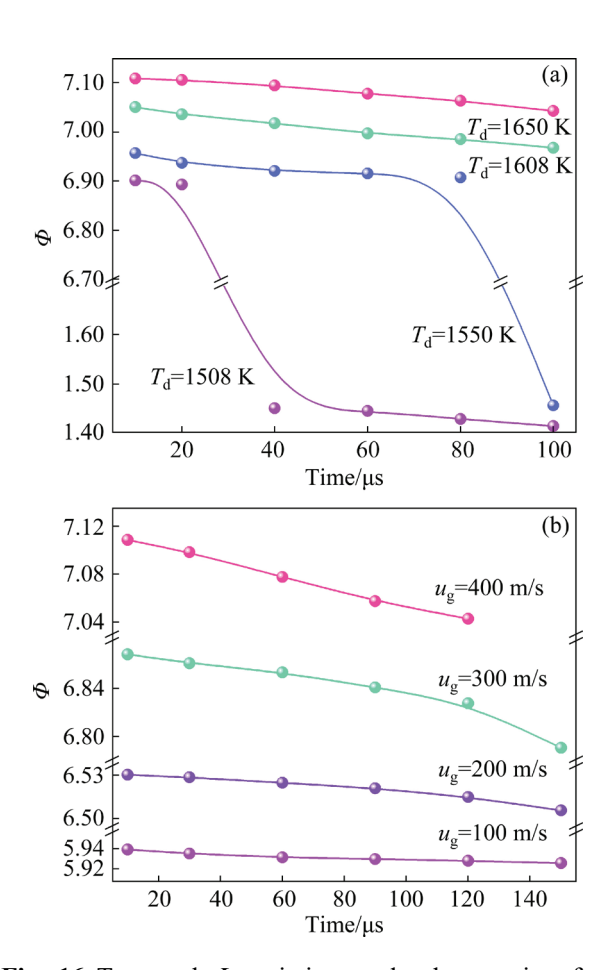


Fig. 16 Temporal Φ variation at droplet–gas interface during droplet deformation and breakup process: (a) At different initial droplet temperatures; (b) At different gas velocities

In summary, Φ decreased upon decreasing the initial droplet temperature or atomizing gas velocity. According to the results in Section 3.2 and Section 3.3, this can facilitate the formation of spherical particles by increasing the droplet temperature or gas velocity, primarily due to the decreased droplet viscous resistance or enhanced aerodynamic driving force for droplet deformation and breakup. Thus, increasing the droplet temperature or gas velocity may promote the production of spherical particles due to the higher ratio of aerodynamic to viscous force.

4.2 Hollow particle formation and evolution

Hollow particles are typical defects of gas-atomized powders and may be one of the major causes of porosity in MAM-formed products [14]. Meanwhile, hot isostatic pressing (HIP) is ineffective for the elimination of large spherical pores in constructed parts by the directed energy deposition of gas-atomized powders with diameters of 50–70 µm [36]. Therefore, the elimination of hollow particles in the metal powder is essential for improving the quality of 3D-printed products. In this study, to trace the source of the porosity defects due to the entrapped atomizing gas in the droplet, it is necessary to examine the typical hollow particle morphology.

Figure 17 presents the SEM micrographs of the typical 316L hollow particles, which primarily include open hollow particles, closed hollow particles, eccentric hollow particles, and bubbledetached hollow particles. Based on the discussion in Section 3.2 and Section 3.3, open hollow particles and closed hollow particles were mainly formed due to the bag or multimode breakup of lower temperature droplets (Figs. 9(b, c)), which is consistent with previous reports [41]. However, for higher-temperature droplets, the lower viscous force results in the formation of a bag film that tends to break, thus avoiding the introduction of hollow particles (Fig. 14(b)). In addition, during the formation of hollow droplets, droplet solidification occurred in the early deformation stages, resulting in the formation of open hollow particles (Fig. 17(a)). If there is a closed hollow bag with the trapped atomizing gas inside that solidifies (Fig. 9(b)), a closed hollow particle can be formed (Fig. 17(b)). However, a closed hollow bag without rapid solidification evolves further.

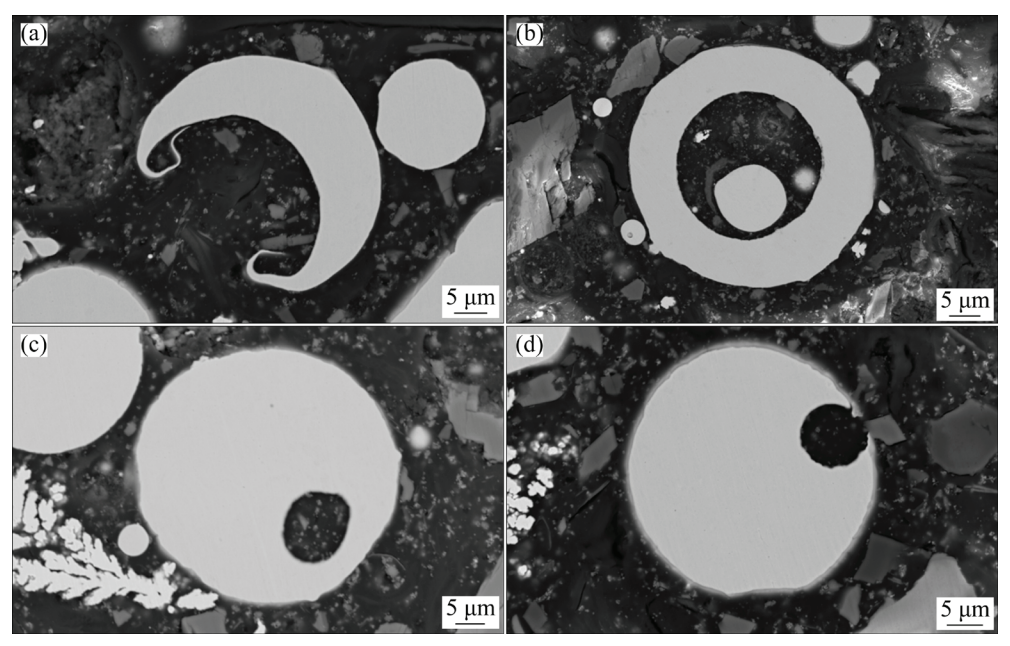


Fig. 17 SEM images showing typical hollow particle morphology: (a) Open hollow particles; (b) Closed hollow particles; (c) Eccentric hollow particles; (d) Bubble-detached hollow particles

Analysis showed that the buoyancy force and Marangoni force acted on the bubble in a droplet, which resulted in a tendency for the bubbles to escape from the droplet as well [11,42]. The pressure inside the spherical gas bubble was balanced by the Laplace pressure arising from surface tension [36]. However, once the spherical gas bubble interface was deformed (Fig. 17(c)), a non-equilibrium Laplace pressure acted as the bubble migration driver due to its asymmetric shape. Finally, this resulted in the formation of eccentric hollow particles and bubble-detached hollow particles (Figs. 17(c, d)). Thus, the complete hollow particle evolution process includes: open hollow film formation, liquid film closure. centrifugation, and bubble detachment. viscous force of the metallic droplets provides resistance to the outward motion of the bubbles. The Marangoni force ($F_{\text{Marangini}}$), buoyancy $(F_{\rm f})$, and Laplace pressure (ΔP) are expressed as follows [43,44]:

$$F_{\text{Marangini}} = \frac{\mathrm{d}\sigma}{\mathrm{d}T} \left(\nabla T - \boldsymbol{n} (\boldsymbol{n} \cdot \nabla T) \right) \tag{15}$$

$$F_{\rm f} = \rho_{\rm g} V g \tag{16}$$

$$\Delta P = \sigma \left(\frac{1}{r_1} + \frac{1}{r_2} \right) \tag{17}$$

where $d\sigma/dT$ is the temperature coefficient of

surface tension, n is the unit normal vector, and r_1 and r_2 are the two orthogonal curvatures of the curved bubble surface, respectively. Marangoni forces were resulted from surface tension gradients due to the non-uniform temperature distribution within the droplet [42], depending on Eq. (15). The bubble deformation caused a smaller variation in the interfacial curvature (Figs. 17(c, d)), whereby the Laplace pressure was also dominated by surface tension around the bubble, depending on Eq. (17). Therefore, the surface tension gradients resulted in bubble migration, including a non-equilibrium Laplace pressure and Marangoni force. These were regulated by non-uniform temperature distribution within the droplet.

To investigate the bubble behavior within the solidified droplet, it is necessary to analyze the root causes of the non-uniform temperature within the droplet. The heat transfer involved in the atomized melt droplets consisted mostly of convection, conduction, and radiation, with convection being dominant [45]. The convective heat density J is given by

$$J=h_{c}(T_{1}-T_{g}) \tag{18}$$

where h_c is the convective coefficient, defined as follows:

$$h_{c} = \frac{k_{g}}{d} (2 + 0.6 \sqrt{\frac{\rho_{g} (u_{g} - u_{d}) d}{u_{g}}} \sqrt{\frac{u_{g} c_{p,g}}{\lambda_{g}}})$$
 (19)

The gas-liquid relative velocity is the key to controlling the convective coefficient. T_1 and T_g are the liquid and gas temperatures, respectively. Figure 18 displays the gas velocity distribution near the gas-liquid interface along the x-axis ($t=10 \mu s$) to disclose the effect of the initial temperature of the melt droplet and the gas velocity on the non-uniform temperature distribution within the droplet. The gas velocity gradient variation at the gas-liquid interface was basically consistent for droplets at different initial temperatures. However, as the gas velocity increased, the gas velocity gradient at the gas-liquid interface significantly increased. By analysis, convective heat transfer where a gas velocity gradient existed at the interface location might have produced non-uniform temperature within the droplet, which was supported by ZHANG et al [46]. A larger gas velocity gradient increased the intensity of convection, resulting in larger regions non-uniform temperatures. This contributed to the development of surface tension gradients. In addition, increasing the droplet temperature has a

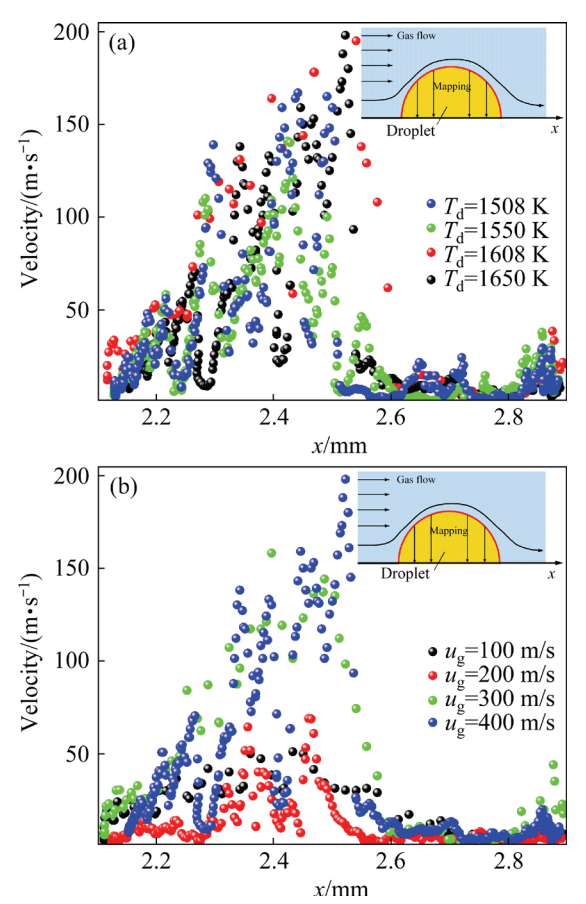


Fig. 18 Gas velocity at gas-liquid interface: (a) At different initial droplet temperatures; (b) At different gas velocities

smaller effect on the convection at the droplet surface, but might result in greater non-uniform temperature distribution within the droplet, as well as a lower viscous force. Therefore, it can be assumed that increasing gas velocity and droplet temperature can enhance bubble migration within the droplet.

In summary, increasing the gas velocity or droplet temperature promoted the migration of bubbles within the hollow droplet in terms of driving or resistance forces. These changes also inhibited the formation of hollow particles. Additionally, the hollow particles were introduced during the droplet breakup stages (Fig. 9(b, c)), which were also affected by the viscous force and aerodynamic force. Higher droplet temperatures and gas velocities also hindered the formation of hollow particles during droplet deformation and fragmentation (Figs. 9 and 14).

5 Conclusions

- (1) A higher droplet temperature or higher gas velocity was more beneficial to the production of spherical particles during droplet breakup, with the origin resting at an increasing ratio of aerodynamic to viscous force.
- (2) A decreasing ratio of aerodynamic to viscous force during droplet breakup resulted in the transformation of the expected breakup mode or only droplet deformation. Therefore, an integrated approach based on *We* and *Oh* is required to assess the metallic droplet breakup mode.
- (3) Hollow particles were mainly formed due to the bag or multimode breakup mode of lower-temperature droplets. The integral hollow particle evolution process included open hollow film formation, liquid film closure, bubble centrifugation, and bubble detachment.
- (4) A lower droplet viscosity and higher gas velocity may help avoid the formation of hollow particles from droplet bags or multimode breakup. Increasing the droplet temperature or gas velocity might facilitate the separation of the bubbles from the droplet due to a reduced viscous force to bubble migration in terms of resistance or improved non-equilibrium Laplace pressure and Marangoni force within melt droplets in terms of driving forces.

CRediT authorship contribution statement

Peng WANG: Conceptualization, Methodology, Validation, Formal analysis, Investigation, Data curation, Writing – Original draft, Writing – Review & editing; Xing-gang LI: Conceptualization, Investigation, Writing - Review & editing, Funding acquisition, Project administration, Supervision; Xiang-lin ZHOU: Conceptualization, Writing - Review & editing, Funding acquisition, Project administration, Supervision; Zhi-pei CHEN: Data curation, Investigation, Validation; Miao-hui WANG: Data curation, Project administration; Ping GAN: Resources, Funding acquisition, Formal analysis; Xiao-na REN: Data curation, Formal analysis; Zhi-yong YU: Supervision, Project administration.

Declaration of competing interest

The authors declare that they have no known competing financial interests or personal relationships that could have appeared to influence the work reported in this paper.

Acknowledgments

This work was financially supported by the National Natural Science Foundation of China (Nos. 51975240, 52074157, 51271034), the National Key Research and Development Program of China (No. 2018YFB0703400), Department of Education of Guangdong Province, China (No. 2023KTSCX121), and Shenzhen Science and Technology Program, China (Nos. JSGG20210802154210032, JCYJ20210324104608023).

References

- [1] XIONG Zhi-wei, LI Hao-hang, YANG Hong, YANG Ying, LIU Yi-nong, CUI Li-shan, LI Xiao-xiao, MASSELING L, SHEN Li-yao-wei, HAO Shi-jie. Micro laser powder bed fusion of NiTi alloys with superior mechanical property and shape recovery function [J]. Additive Manufacturing, 2022, 57: 102960.
- [2] YAO Li-ming, HUANG Sheng, RAMAMURTY U, XIAO Zhong-min. On the formation of "Fish-scale" morphology with curved grain interfacial microstructures during selective laser melting of dissimilar alloys [J]. Acta Materialia, 2021, 220: 117331.
- [3] YURTKURAN E, RAHMI Ü. Theoretical and experimental investigation of Ti alloy powder production using low-power plasma torches [J]. Transactions of Nonferrous Metals Society of China, 2022, 32(1): 175–191.
- [4] YAO Deng-zhi, LIU Xiao-han, WANG Ju, FAN Wei, LI Meng, FU Hai-tao, ZHANG Hao, YANG Xiao-hong, ZOU Qing-chuan, AN Xi-zhong. Numerical insights on the spreading of practical 316 L stainless steel powder in SLM additive manufacturing [J]. Powder Technology, 2021, 390: 197–208.

- [5] YAO Deng-zhi, AN Xi-zhong, FU Hai-tao, ZHANG Hao, YANG Xiao-hong, ZOU Qing-chuan, DONG Ke-jun. Dynamic investigation on the powder spreading during selective laser melting additive manufacturing [J]. Additive Manufacturing, 2021, 37: 101707.
- [6] DING Wang-wang, CHEN Gang, QIN Ming-li, HE Yue-hui, QU Xuan-hui. Low-cost Ti powders for additive manufacturing treated by fluidized bed [J]. Powder Technology, 2019, 350: 117–122.
- [7] LI Xing-gang, ZHU Qiang, SHU Shi, FAN Jian-zhong, ZHANG Shao-ming. Fine spherical powder production during gas atomization of pressurized melts through melt nozzles with a small inner diameter [J]. Powder Technology, 2019, 356: 759–768.
- [8] CUI Yu-jie, ZHAO Yu-fan, NUMATA H, YAMANAKA K, BIAN Hua-kang, AOYAGI K, CHIBA A. Effects of process parameters and cooling gas on powder formation during the plasma rotating electrode process [J]. Powder Technology, 2021, 393: 301–311.
- [9] SAMES W J, LIST F A, PANNALA S, DEHOFF R R, BABU S S. The metallurgy and processing science of metal additive manufacturing [J]. International Materials Reviews, 2016, 61(5): 315–360.
- [10] SHI Yu-tong, LU Wei-yan, SUN Wen-hai, ZHANG Suo-de, YANG Bai-jun, WANG Jian-qiang. Impact of gas pressure on particle feature in Fe-based amorphous alloy powders via gas atomization: Simulation and experiment [J]. Journal of Materials Science & Technology, 2022, 105: 203–213.
- [11] LUO Sheng, WANG Hong-ze, GAO Zhen-yang, WU Yi, WANG Hao-wei. Interaction between high-velocity gas and liquid in gas atomization revealed by a new coupled simulation model [J]. Materials & Design, 2021, 212: 110264.
- [12] LU Yun-zhuo, ZHANG Hao, LI Hong-ge, XU Hui-dong, HUANG Guo-kun, QIN Zuo-xiang, LU Xing. Crystallization prediction on laser three-dimensional printing of Zr-based bulk metallic glass [J]. Journal of Non-Crystalline Solids, 2017, 461: 12–17.
- [13] LUO Sheng, OUYANG Yu, WEI Qiang-long, LAI Shu-yue, WU Yi, WANG Hao-wei, WANG Hong-ze. Understanding the breakup behaviors of liquid jet in gas atomization for powder production [J]. Materials & Design, 2023, 227: 111793.
- [14] ANDERSON I E, WHITE E M H, DEHOFF R. Feedstock powder processing research needs for additive manufacturing development [J]. Current Opinion in Solid State and Materials Science, 2018, 22(1): 8–15.
- [15] STEFANITSIS D, STROTOS G, NIKOLOPOULOS N, KAKARAS E, GAVAISES M. Improved droplet breakup models for spray applications [J]. International Journal of Heat and Fluid Flow, 2019, 76: 274–286.
- [16] JAIN S S, TYAGI N, PRAKASH R S, RAVIKRISHNA R V, TOMAR G. Secondary breakup of drops at moderate Weber numbers: Effect of density ratio and reynolds number [J]. International Journal of Multiphase Flow, 2019, 117: 25–41.
- [17] CHEN Yi, WAGNER J L, FARIAS P A, DEMAURO E P, GUILDENBECHER D R. Galinstan liquid metal breakup and droplet formation in a shock-induced cross-flow [J]. International Journal of Multiphase Flow, 2018, 106:

147-163.

- [18] RIDOLFI M R, FOLGARAIT P. Numerical modeling of secondary breakup in molten metals gas-atomization using dimensionless analysis [J]. International Journal of Multiphase Flow, 2020, 132: 103431.
- [19] JACKIW I M, ASHGRIZ N. On aerodynamic droplet breakup [J]. Journal of Fluid Mechanics, 2021, 913: A33.
- [20] HOPFES T, PETERSEN J, WANG Z, GIGLMAIER M, ADAMS N A. Secondary atomization of liquid metal droplets at moderate weber numbers [J]. International Journal of Multiphase Flow, 2021, 143: 103723.
- [21] KAISER R, LI Cheng-guo, YANG Sang-sun, LEE D. A numerical simulation study of the path-resolved breakup behaviors of molten metal in high-pressure gas atomization: With emphasis on the role of shock waves in the gas/molten metal interaction [J]. Advanced Powder Technology, 2018, 29(3): 623-630.
- [22] ARACHCHILAGE K H, HAGHSHENAS M, PARK S, ZHOU Le, SOHN Y, MCWILLIAMS B, CHO K, KUMAR R. Numerical simulation of high-pressure gas atomization of two-phase flow: Effect of gas pressure on droplet size distribution [J]. Advanced Powder Technology, 2019, 30(11): 2726–2732.
- [23] WEI Ming-wei, CHEN Sui-yuan, SUN Miao, LIANG Jing, LIU Chang-sheng, WANG Mei. Atomization simulation and preparation of 24CrNiMoY alloy steel powder using VIGA technology at high gas pressure [J]. Powder Technology, 2020, 367: 724–739.
- [24] KIRMSE C, CHAVES H. Measurement of the average two-dimensional surface temperature distribution of drops in a melt atomization process [J]. Journal of Thermal Spray Technology, 2015, 24: 690–695.
- [25] LIU Chang, LI Xin, SHU Shi, HUANG Yu-he, LI Xing-gang, ZHU Qiang. Numerical investigation on flow process of liquid metals in melt delivery nozzle during gas atomization process for fine metal powder production [J]. Transactions of Nonferrous Metals Society of China, 2021, 31(10): 3192–3204.
- [26] WAN Zhang-hao, YANG Shi-liang, KONG De-song, LI Dong-bo, HU Jian-hang, WANG Hua. Numerical modelling of stirring characteristics of gas—slag—copper matte multiphase flow in bath with top submerged lance [J]. Transactions of Nonferrous Metals Society of China, 2023, 33(7): 2231–2244.
- [27] LI Xing-gang, FRITSCHING U. Process modeling pressureswirl-gas-atomization for metal powder production [J]. Journal of Materials Processing Technology, 2017, 239: 1–17.
- [28] GUILDENBECHER D R, LÓPEZ-RIVERA C, SOJKA P E. Secondary atomization [J]. Experiments in Fluids, 2009, 46(3): 371–402.
- [29] CAO Liu. Workpiece-scale numerical simulations of SLM molten pool dynamic behavior of 316L stainless steel [J]. Computers & Mathematics with Applications, 2021, 96: 209–228.
- [30] HU Yun-fei, ZHOU Xiang-lin, XU Liang-hui, LI Jing-hao, QI Hang, DU Kai-ping, MA Yao, YU Yue-guang. Motion and solidification behavior analysis of Fe-based alloy droplets during gas atomization [J]. Metallurgical and

- Materials Transactions B, 2020, 51: 2935-2945.
- [31] SHARMA S, SINGH A P, RAO S S, KUMAR A, BASU S. Shock induced aerobreakup of a droplet [J]. Journal of Fluid Mechanics, 2021, 929: A27.
- [32] WANG Peng, LI Jing, WANG Xin, LIU Heng-san, FAN Bin, GAN Ping, GUO Rui-feng, GE Xue-yuan, WANG Miao-hui. Close-coupled nozzle atomization integral simulation and powder preparation using vacuum induction gas atomization technology [J]. Chinese Physics B, 2021, 30(2): 027502.
- [33] ALMANGOUR B, GRZESIAK D, CHENG Jin-quan, ERTAS Y. Thermal behavior of the molten pool, microstructural evolution, and tribological performance during selective laser melting of TiC/316L stainless steel nanocomposites: Experimental and simulation methods [J]. Journal of Materials Processing Technology, 2018, 257: 288–301.
- [34] WANG Jun-feng, XIA Min, WU Jia-lun, GE Chang-chun. Ladle nozzle clogging in vacuum induction melting gas atomization: Influence of the melt viscosity [J]. Metallurgical and Materials Transactions B, 2022, 53: 2386–2397.
- [35] HSIANG L P, FAETH G M. Drop deformation and breakup due to shock wave and steady disturbances [J]. International Journal of Multiphase Flow, 1995, 21(4): 545–560.
- [36] RABIN B H, SMOLIK G R, KORTH G E. Characterization of entrapped gases in rapidly solidified powders [J]. Materials Science and Engineering A, 1990, 124: 1–7.
- [37] SEE J B, JOHNSTON G H. Interactions between nitrogen jets and liquid lead and tin streams [J]. Powder Technology, 1978, 21: 119–133.
- [38] BECKERS D, ELLENDT N, FRITSCHING U, UHLENWINKEL V. Impact of process flow conditions on particle morphology in metal powder production via gas atomization [J]. Advanced Powder Technology, 2020, 31(1): 300–311.
- [39] URIONABARRENETXEA E, MARTÍN J M, AVELLO A, RIVAS A. Simulation and validation of the gas flow in close-coupled gas atomisation process: Influence of the inlet gas pressure and the throat width of the supersonic gas nozzle [J]. Powder Technology, 2022, 407: 117688.
- [40] CHEN Gang, YANG Xian, SU Bin, TU Chuan-jun. Criterion of gas and solid dual-phase flow atomization crash in molten metal [J]. Transactions of Nonferrous Metals Society of China, 2014, 24(1): 208–216.
- [41] XIONG Liang-hua, CHUANG A C, THOMAS J, PROST T, WHITE E, ANDERSON I, SINGH D. Defect and satellite characteristics of additive manufacturing metal powders [J]. Advanced Powder Technology, 2022, 33(3): 103486.
- [42] HUANG Wen-kang, WANG Hong-liang, RINKER T, TAN Wen-da. Investigation of metal mixing in laser keyhole welding of dissimilar metals [J]. Materials & Design, 2020, 195: 109056.
- [43] MENG Qing-bo, ZHOU Xiang-lin, LI Jing-hao, CUI Zi-qi, WANG Yan-dong, ZHANG Hai-long, LI Zhuo, QIU Chun-lei. High-throughput laser fabrication of Ti-6Al-4V alloy: Part I. Numerical investigation of dynamic behavior in molten pool [J]. Journal of Manufacturing Processes, 2020, 59: 509-522.
- [44] WANG Zhan-long, WANG Xiao-he, MIAO Qing, ZHAO Ya-pu. Realization of self-rotating droplets based on liquid

- metal [J]. Advanced Materials Interfaces, 2021, 8(3): 2001756.
- [45] SHI Y T, LU W Y, SUN W H, ZHANG S D, YANG B J, WANG J Q. Pressure-dependent microstructure evolution of Fe-based amorphous alloy powders via high-pressure gas
- atomization [J]. Journal of Alloys and Compounds, 2022, 920: 166038.
- [46] ZHANG Min, ZHANG Zhao-ming. Numerical simulation study on cooling of metal droplet in atomizing gas [J]. Materials Today Communications, 2020, 25: 101423.

气体雾化过程中涉及颗粒形貌和空心颗粒形成的 金属液滴变形和破碎数值模拟

汪鹏^{1,2},黎兴刚³,周香林¹,陈志培⁴,王淼辉²,甘萍²,任晓娜⁴,余志勇⁵

- 1. 北京科技大学 新金属材料国家重点实验, 北京 100083;
 - 2. 中机新材料研究院(郑州)有限公司,郑州 450001;
 - 3. 南方科技大学 材料科学与工程系,深圳 518055;
 - 4. 北京科技大学 材料科学与工程学院, 北京 100083;
 - 5. 中国联合重型燃气轮机技术有限公司, 北京 100016

摘 要:采用考虑液滴冷却和凝固的流体体积(VOF)方法模拟金属液滴在气体雾化过程中的变形和破碎。建立典型粉末形貌和液滴破碎行为之间的相关性,以指导球形粉末颗粒的制备。结果显示,当增加液滴的气动力与黏性力的比值时,球形颗粒的形成得到加强;然而,当减小这个比值时,预期的液滴破碎模型将被改变或仅仅只发生液滴的变形。从空心颗粒的形成和演变过程的数值模拟中观察到几种典型的情况,例如,开放的空心液膜的形成、液膜封闭、气泡的离心和气泡的脱离。通过提高气体速度或液滴温度,实现较高的非平衡拉普拉斯压力或较低的粘性力,促使气泡从液滴内部分离。

关键词:液滴破碎;空心颗粒;颗粒形貌;黏性力;金属粉末;气体雾化

(Edited by Bing YANG)